

Cooling of Superfluid Neutron Stars

D.G. Yakovlev¹, O.Y. Gnedin², A.D. Kaminker¹, and A.Y. Potekhin¹

¹ Ioffe Physical Technical Institute, Politekhnikeskaya 26, 194021 St. Petersburg, Russia

² Space Telescope Science Institute, 3700 San Martin Drive, Baltimore, MD 21218, USA
 yak@astro.ioffe.rssi.ru, ognedin@stsci.edu, kam@astro.ioffe.rssi.ru, palex@astro.ioffe.rssi.ru

Abstract. Cooling of neutron stars (NSs) with the cores composed of neutrons, protons, and electrons is analyzed. The main cooling regulators are discussed: opening of direct Urca process in a NS central kernel; superfluidity of nucleons in NS interiors; surface layers of light (accreted) elements; strong surface magnetic fields. An emphasis is paid on the cooling scenario with strong 1S_0 pairing of protons and weak 3P_2 pairing of neutrons in the NS core, as well as strong 1S_0 pairing of neutrons in the NS crust. The theory predicts three types of isolated cooling middle-aged NSs with distinctly different properties: low-mass, slowly cooling NSs; medium-mass, moderately cooling NSs; massive, rapidly cooling NSs. The theory is compared with observations of isolated NSs — pulsars and radio quiet NSs in supernova remnants. The constraints on physical properties of NSs which can be inferred from such a comparison are outlined.

1. Introduction

Cooling of neutron stars (NSs) depends on the properties of dense matter in their crusts and cores. These properties are still poorly known and cannot be described unambiguously by contemporary theories. For instance, calculations of the equation of state (EOS) of the NS cores (e.g., Latimer & Prakash 2001) or the superfluid properties of NS cores and crusts (e.g., Lombardo & Schulze 2001) give a large scatter of results which depend on a model of strong interaction and a many-body theory employed. However, these properties can be studied by comparing the results of simulations of NS cooling with the observations of thermal emission from isolated NSs. We will describe some recent results of such studies. The history of NS cooling theory is reviewed, for instance, by Yakovlev et al. (1999)

For simplicity, we consider the NS models with the cores composed mainly of neutrons with an admixture of protons and electrons. We discuss the basic ideas of the cooling theory, and the main cooling regulators, paying special attention on the effects of superfluidity of nucleons in NS interiors. Our consideration will be based on recent simulations of the cooling of superfluid NSs by Kaminker

et al. (2001), Potekhin & Yakovlev (2001), Yakovlev et al. (2001b), and Kaminker et al. (2002, hereafter KYG).

2. Equations of thermal evolution

Neutron stars are born very hot in supernova explosions, with internal temperature $T \sim 10^{11}$ K, but gradually cool down. In about 30 s after the birth a star becomes fully transparent for neutrinos generated in its interiors. We consider the cooling in the following neutrino-transparent stage. The cooling is realized via two channels, by neutrino emission from the entire stellar body and by heat transport from the internal layers to the surface resulting in the thermal emission of photons. For simplicity, we neglect the possible reheating mechanisms (frictional dissipation of rotational energy, or Ohmic decay of internal magnetic field, or the dissipation associated with weak deviations from the chemical equilibrium as reviewed, e.g., by Page 1998).

The internal structure of NSs can be regarded as temperature-independent (e.g., Shapiro & Teukolsky 1983). The general relativistic equations of thermal evolution include the energy and flux equations obtained by Thorne (1977). For a spherically symmetric NS,

$$\frac{1}{4\pi r^2 e^{2\Phi}} \sqrt{1 - \frac{2Gm}{c^2 r}} \frac{\partial}{\partial r} (e^{2\Phi} L_r) = -Q - \frac{c_v}{e^\Phi} \frac{\partial T}{\partial t}, \quad (1)$$

$$\frac{L_r}{4\pi \kappa r^2} = -\sqrt{1 - \frac{2Gm}{c^2 r}} e^{-\Phi} \frac{\partial}{\partial r} (T e^\Phi), \quad (2)$$

where Q is the neutrino emissivity [$\text{erg cm}^{-3} \text{s}^{-1}$], c_v is the heat capacity per cm^3 [$\text{erg cm}^{-3} \text{K}^{-1}$], κ is the thermal conductivity [$\text{erg cm}^{-1} \text{s}^{-1} \text{K}^{-1}$], and L_r is the “local luminosity” [erg s^{-1}] defined as the non-neutrino heat flux transported through a sphere of radius r . The gravitational mass $m(r)$ and the metric function $\Phi(r)$ are determined by the stellar model.

It is conventional (e.g., Gudmundsson et al. 1983) to subdivide the calculation of heat transport in the neutron-star interior ($r < R_b$) and in the outer heat-blanketing envelope ($R_b \leq r \leq R$), where R is the stellar radius, and the boundary radius R_b corresponds to the density

$\rho_b \sim 10^{10} \text{ g cm}^{-3}$ (~ 100 meters under the surface). In the presence of superstrong surface magnetic field, it is reasonable to shift ρ_b to the neutron drip density, $4 \times 10^{11} \text{ g cm}^{-3}$ (Potekhin & Yakovlev 2001). The thermal structure of the blanketing envelope is studied separately in the stationary, plane-parallel approximation to relate the effective surface temperature T_s to the temperature T_b at the inner boundary of the envelope. We discuss the T_s – T_b relation in Sect. 3. It is used as the boundary condition for solving Eqs. (1) and (2) at $r < R_b$.

The effective temperature determines the photon luminosity $L_\gamma = 4\pi\sigma R^2 T_s^4(t)$. Both, L_γ and T_s refer to the locally-flat reference frame on the surface. A distant observer would register the “apparent” luminosity $L_\gamma^\infty = L_\gamma(1 - r_g/R)$ and the “apparent” effective temperature $T_s^\infty = T_s \sqrt{1 - r_g/R}$, where $r_g = 2GM/c^2$ is the Schwarzschild radius and $M = m(R)$ is the total gravitational mass.

The main goal of the cooling theory is to calculate *cooling curves*, $T_s^\infty(t)$, to be compared with observations. One can distinguish three main cooling stages: (i) the internal relaxation stage ($t \lesssim 10$ – 100 yr; Lattimer et al. 1994; Gnedin et al. 2001), (ii) the neutrino cooling stage (the neutrino luminosity $L_\nu \gg L_\gamma$, $t \lesssim 10^5$ yr), and (iii) the photon cooling stage ($L_\nu \ll L_\gamma$, $t \gtrsim 10^5$ yr).

After the thermal relaxation, the redshifted temperature $\tilde{T}(t) = T(r, t) e^{\Phi(r)}$ becomes constant throughout the stellar interior. Then Eqs. (1) and (2) reduce to the equation of global thermal balance,

$$C(\tilde{T}) \frac{d\tilde{T}}{dt} = -L_\nu^\infty(\tilde{T}) - L_\gamma^\infty(T_s), \quad (3)$$

$$L_\nu^\infty(\tilde{T}) = 4\pi \int_0^{R_b} \frac{dr r^2 Q(\tilde{T}) e^{2\Phi}}{\sqrt{1 - 2Gm/(c^2 r)}}, \quad (4)$$

$$C(\tilde{T}) = 4\pi \int_0^{R_b} \frac{dr r^2 c_v(\tilde{T})}{\sqrt{1 - 2Gm/(c^2 r)}}, \quad (5)$$

where C is the total NS heat capacity, and L_ν^∞ is the total neutrino luminosity.

3. Physics input

We describe the results obtained using a fully relativistic non-isothermal cooling code (Gnedin et al. 2001). The code solves the heat diffusion equations (Sect. 2) in the NS interior.

The physics input is as follows. The EOS in the NS crust is taken from Negele & Vautherin (1973) (assuming spherical atomic nuclei everywhere in the crust). The core-crust boundary is placed at the density $1.5 \times 10^{14} \text{ g cm}^{-3}$. In the core, we use two phenomenological EOSs (EOS A and EOS B) proposed by Prakash et al. (1988).

EOS A is model I of Prakash et al. (1988) with the compression modulus of saturated nuclear matter $K = 240 \text{ MeV}$. EOS B corresponds to $K = 180 \text{ MeV}$ and to

Table 1. NS models employing EOSs A and B (from KYG)

Model	Main parameters	EOS A	EOS B
Maximum mass model	M_{max}/M_\odot	1.977	1.73
	$\rho_{\text{cmax}}/10^{14} \text{ g cm}^{-3}$	25.75	32.5
	$R \text{ km}$	10.754	9.71
Direct Urca threshold model	M_D/M_\odot	1.358	1.44
	$\rho_D/10^{14} \text{ g cm}^{-3}$	7.851	12.98
	$R \text{ km}$	12.98	11.54

the simplified form of the symmetry energy suggested by Page & Applegate (1992). It has been used in many papers (e.g., Page & Applegate 1992, Yakovlev et al. 1999, 2001a, and references therein).

The masses, central densities, and radii of two stellar configurations for EOSs A and B are given in Table 1. The first configuration corresponds to the maximum-mass NS. The values of M_{max} reveal that EOS A is stiff, and EOS B is moderate. The second configuration has a central density ρ_c at which the direct Urca process switches on (the process is allowed at $\rho_c > \rho_D$, which corresponds to $M > M_D$). EOS B is based on a smaller symmetry energy and opens the direct Urca process at a higher ρ .

The cooling code includes all important neutrino emission processes in the NS core (direct and modified Urca processes, neutrino bremsstrahlung in nucleon-nucleon scattering, neutrino emission due to Cooper pairing of nucleons) and in the crust (plasmon decay, neutrino bremsstrahlung due to scattering of electrons off atomic nuclei, electron-positron annihilation into neutrino pairs, neutrino emission due to Cooper pairing of neutrons in the inner crust). These processes are reviewed, for instance, by Yakovlev et al. (2001a). The effective masses of protons and neutrons in the core and free neutrons in the crust are taken to be 0.7 of the bare nucleon masses. The values of the thermal conductivity in the NS crust and core are the same as used by Gnedin et al. (2001).

The T_s – T_b relationship is taken from Potekhin et al. (1997) and Potekhin & Yakovlev (2001). It is relevant either for the surface layers made of iron (without any magnetic field and with the dipole surface magnetic fields $B \lesssim 10^{15} \text{ G}$), or for the non-magnetic surface layers containing light elements. In addition, we have modified the relationship by incorporating our new results which take into account the combined effects of accreting envelopes and magnetic fields. It is assumed that the surface magnetic field induces an anisotropic heat transport in the heat-blanketing envelope but does not violate the isotropic (radial) heat diffusion in the deeper NS layers. This preserves the scheme of solving the radial heat diffusion equations (Sect. 2). In this case, T_s varies over the NS surface, and the cooling theory deals with the mean surface temperature \bar{T}_s that determines the NS photon luminosity. For brevity, we denote \bar{T}_s as T_s . It is also assumed that

Table 2. Parameters of superfluid models in Eq. (6); from KYG

Pair- ing	Mo- del	$T_0/10^9$ K	k_0 fm^{-1}	k_1 fm^{-1}	k_2 fm^{-1}	k_3 fm^{-1}
1S_0	1p	20.29	0	1.117	1.241	0.1473
1S_0	2p	17	0	1.117	1.329	0.1179
1S_0	3p	14.5	0	1.117	1.518	0.1179
1S_0	1ns	10.2	0	0.6	1.45	0.1
1S_0	2ns	7.9	0	0.3	1.45	0.01
1S_0	3ns	1800	0	21	1.45	0.4125
3P_2	1nt	6.461	1	1.961	2.755	1.3

a NS may have a hydrogen atmosphere even if the heat-blanketing envelope is mostly made of iron. The majority of cooling curves are calculated for the non-magnetized heat-blanketing envelopes made of iron. The exceptions are discussed in Sect. 6.3.

We will focus on the effects of nucleon superfluidity on NS cooling. The superfluid properties of NS matter are characterized by the density-dependent critical temperatures $T_c(\rho)$ of nucleons. Microscopic theories predict (e.g., Lombardo & Schulze 2001, Yakovlev et al. 1999) superfluidities of three types: singlet-state (1S_0) pairing of neutrons ($T_c = T_{\text{cns}}$) in the inner crust and outermost core; 1S_0 proton pairing ($T_c = T_{\text{cp}}$) in the core; and triplet-state (3P_2) neutron pairing ($T_c = T_{\text{cnt}}$) in the core. Superfluidity of nucleons suppresses neutrino processes involving nucleons, initiates a specific mechanism of neutrino emission associated with Cooper pairing of nucleons (Flowers et al. 1976), and affects the nucleon heat capacity. All these effects are incorporated into the cooling code as described by Yakovlev et al. (1999, 2001a) and Gnedin et al. (2001).

The microscopic calculations of superfluid critical temperatures $T_c(\rho)$ give a large scatter of results (e.g., Lombardo & Schulze 2001), but some common features are clear. For instance, $T_c(\rho)$ increases with ρ at sufficiently low densities (due to an increasing strength of the attractive part of nucleon-nucleon interaction), reaches maximum and then decreases (due to a short-range nucleon-nucleon repulsion), vanishing at a rather high density. For $T_{\text{cns}}(\rho)$, the maximum occurs at sub-nuclear densities, while the switch off takes place at $\rho \sim \rho_0$, where $\rho_0 \approx 2.8 \times 10^{14} \text{ g cm}^{-3}$ is the saturated nuclear matter density. For $T_{\text{cp}}(\rho)$ and $T_{\text{cnt}}(\rho)$, the maxima take place at a few ρ_0 and the fall occurs at the densities several times higher. The maximum values of T_c range from about 10^8 K (or even lower) to $(2-3) \times 10^{10}$ K, depending on the microscopic theoretical model. The maximum values of T_{cnt} are typically lower than those of T_{cp} and T_{cns} , due to the weaker nucleon-nucleon attraction in the 3P_2 state.

Instead of studying T_c as a function of ρ , it is often convenient to consider T_c as a function of the nucleon Fermi wavenumber $k = k_{\text{FN}} = (3\pi^2 n_N)^{1/3}$, where n_N is the number density of nucleon species N=n or p (neutrons or pro-

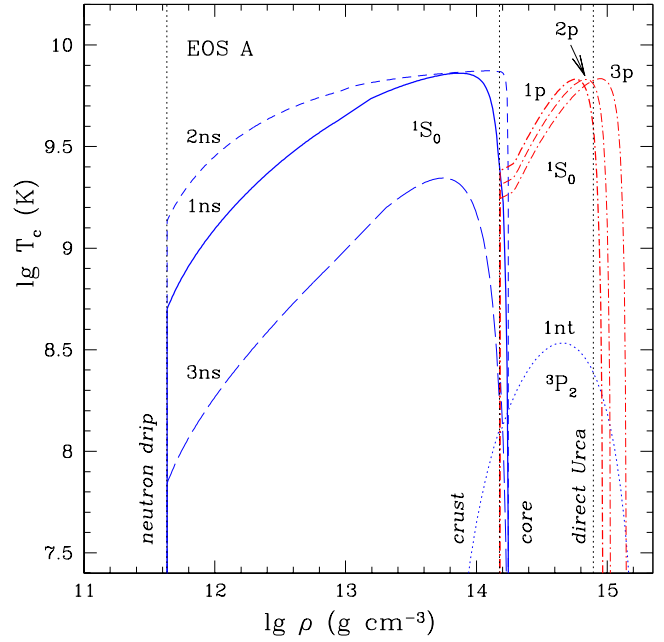


Fig. 1. Density dependence (from KYG) of the critical temperatures for three models 1p, 2p, and 3p of the proton superfluidity (dots-and-dashes) in the core (with EOS A); three models 1ns, 2ns, and 3ns of 1S_0 neutron superfluidity (solid, short-dashed, and long-dashed lines); and one model 1nt of 3P_2 neutron superfluidity (dots) used in cooling simulations. Vertical dotted lines indicate the neutron drip point, core-crust interface, and direct Urca threshold.

tons). Moreover, instead of $T_c(k)$ one often considers $\Delta(k)$, the zero-temperature superfluid gap. For the 1S_0 pairing, assuming BCS theory, one has $\Delta(k) = T_c(k)/0.5669$. In the case of 3P_2 neutron pairing, the gap depends on the orientation of nucleon momenta with respect to the quantization axis. Following the majority of papers, we adopt the 3P_2 pairing with zero projection of the total angular momentum on the quantization axis. In that case $\Delta_{\text{nt}}(k) = T_{\text{cnt}}(k)/0.8416$, where $\Delta_{\text{nt}}(k)$ is the minimum value of the gap on the neutron Fermi surface (e.g., Yakovlev et al. 1999). The dependence of the gaps on k for the selected superfluidity models is plotted in KYG.

Taking into account large scatter of theoretical values of $T_c(k)$ it is instructive to consider $T_c(k)$ as unknown functions and analyze (Sect. 6) which of them are consistent with observations. In this paper, following KYG, we adopt the parameterization of T_c of the form:

$$T_c = T_0 \frac{(k - k_0)^2}{(k - k_0)^2 + k_1^2} \frac{(k - k_2)^2}{(k - k_2)^2 + k_3^2}, \quad (6)$$

for $k_0 < k < k_2$; and $T_c = 0$, for $k \leq k_0$ or $k \geq k_2$. The factor T_0 regulates the amplitude of T_c , k_0 and k_2 determine positions of the low- and high-density cutoffs, while k_1 and k_3 specify the shape of $T_c(\rho)$. All wave numbers, k, k_0, \dots, k_3 are expressed in fm^{-1} . KYG verified that by

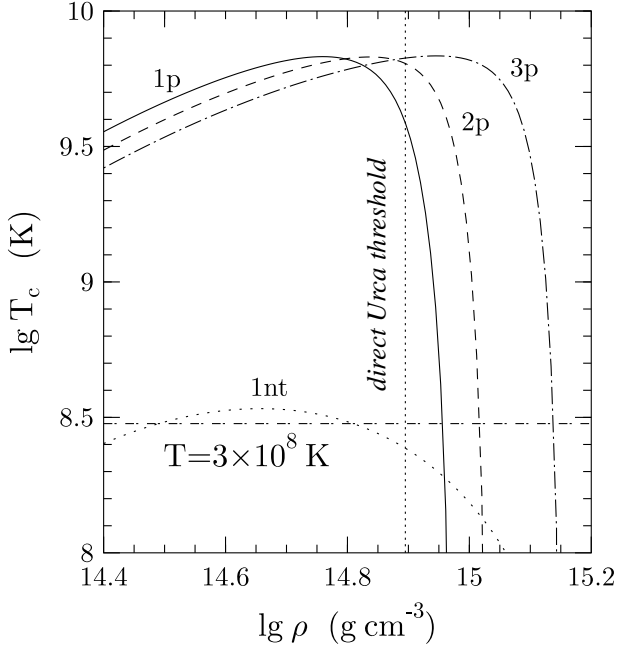


Fig. 2. Density dependence of the critical temperatures of superfluidity of protons (models 1p, 2p, and 3p — solid, dashed, and dot-and-dashed lines) and neutrons (model 1nt — dotted line) in the NS core for EOS A on a larger scale than in Fig. 1. Vertical dotted line indicates direct Urca threshold. Horizontal line is the temperature of matter, $T = 3 \times 10^8$ K, adopted in Fig. 3.

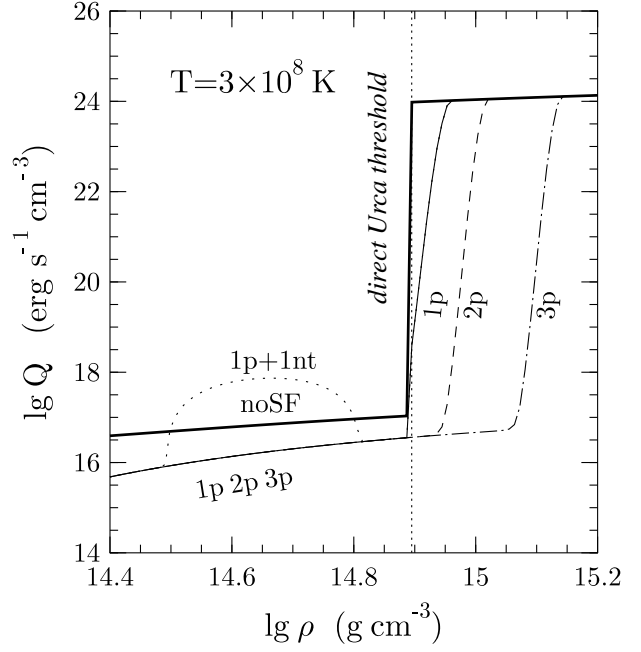


Fig. 3. Density dependence of the neutrino emissivity Q in the NS core at $T = 3 \times 10^8$ K and EOS A. Solid, dashed and dot-and-dashed lines 1p, 2p, and 3p are plotted for proton superfluidity models displayed in Fig. 2. The dotted line shows Q in the presence of proton superfluidity 1p and neutron superfluidity 1nt. The thick solid line is Q in non-superfluid matter.

tuning T_0, k_0, \dots, k_3 , the parameterization accurately describes numerous results of microscopic calculations.

Following KYG we use three models of 1S_0 proton superfluidity, three models of 1S_0 neutron superfluidity, and one model of 3P_2 neutron superfluidity. The parameters of the models are given in Table 2, and the appropriate $T_c(\rho)$ are plotted in Figs. 1, 2, and 4. One has $k_0 = 0$ for 1S_0 pairing. At any given ρ it is reasonable to choose the neutron superfluidity (1S_0 or 3P_2) with higher T_c .

Models 1ns and 2ns of neutron pairing in the crust correspond to about the same, rather strong superfluidity (with maximum $T_{\text{cns}} \approx 7 \times 10^9$ K). Model 2ns has flatter maximum and sharper decreasing slopes in the wings (near the crust-core interface and the neutron drip point). Model 3ns represents a much weaker superfluidity, with maximum $T_{\text{cns}} \approx 2.4 \times 10^9$ K and a narrower density profile.

The proton superfluidity curves 1p, 2p, and 3p in Figs. 1 and 2 are similar. The maximum values of T_{cp} are about 7×10^9 K for all three models. The models differ by the positions of the maximum and decreasing slopes of $T_{\text{cp}}(\rho)$. The decreasing slope of model 1p is slightly above the threshold density of the direct Urca process (for EOS A), while the slopes for models 2p and 3p are shifted to higher ρ . Our models 1p, 2p, and 3p are typical for those micro-

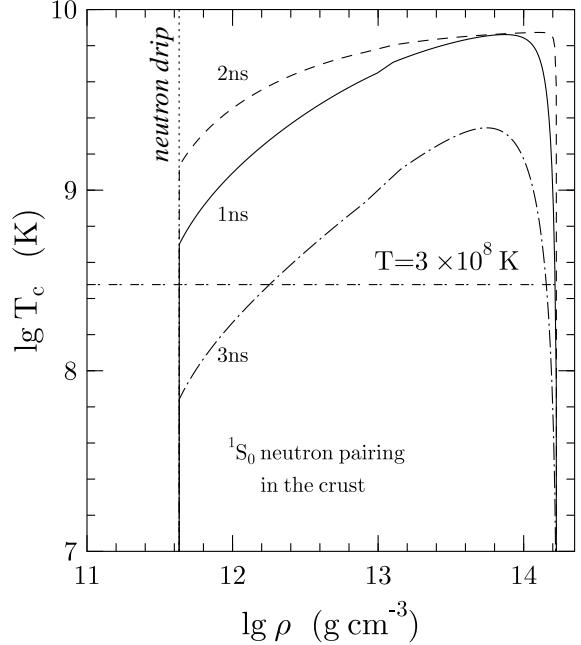


Fig. 4. Density dependence of the critical temperatures of superfluidity of neutrons (models 1ns, 2ns, and 3ns) in the NS crust (cf. Fig. 1). Vertical dotted line indicates neutron drip point. Horizontal line is the temperature of matter, $T = 3 \times 10^8$ K, adopted in Fig. 5.

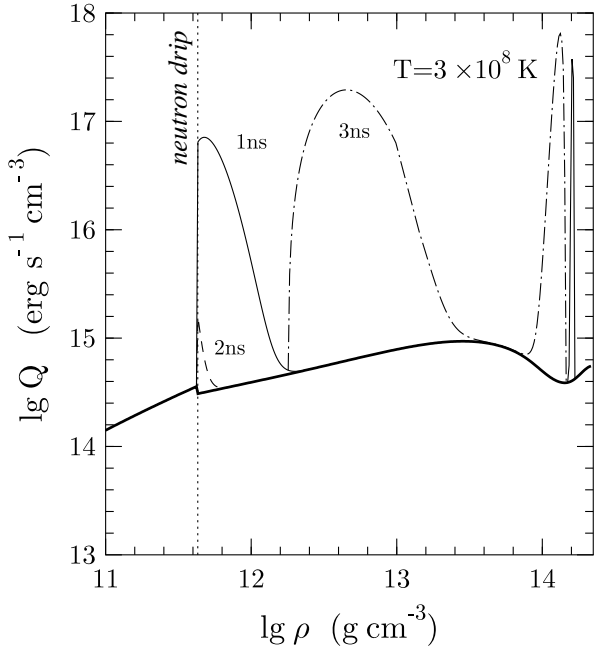


Fig. 5. Density dependence of the neutrino emissivity Q in the NS crust at $T = 3 \times 10^8$ K. Thin solid, dashed, and dot-and-dashed lines 1ns, 2ns, and 3ns are calculated for neutron superfluidity models displayed in Fig. 4. The thick solid line is for non-superfluid matter. The core-crust boundary is artificially shifted to higher ρ for a better visualization of the effects of neutrino emission associated with 1S_0 Cooper pairing of neutrons.

scopic theories which adopt a moderately strong medium polarization of proton-proton interaction.

Finally, the dotted curve in Figs. 1 and 2 shows $T_{\text{cnt}}(\rho)$ for 1nt model of 3P_2 neutron pairing (used by Kaminker et al. 2001). The curve falls within a wide scatter of $T_{\text{cnt}}(\rho)$, provided by microscopic theories.

4. Main regulators of neutron-star cooling

Theoretical cooling curves depend on many features of NS models. Below we discuss four main regulators of the cooling of middle-aged NSs: (1) central kernels, where neutrino emission is enhanced by direct Urca process; (2) the effects of nucleon superfluidity on neutrino emission; (3) surface envelopes of light elements; and (4) surface magnetic fields. The effects of these factors are illustrated in Figs. 2–7. The effects (1) and (2) are the strongest, although (3) and (4) can also be important.

4.1. Direct Urca process in non-superfluid NSs

The NS cooling is strongly affected by the presence of the central NS kernels ($\rho > \rho_D$, Table 1), where direct Urca process – the most powerful neutrino emission mechanism – is open. The effect is especially pronounced in the absence of nucleon superfluidity. For instance, Fig. 3 shows

the density profile of the total neutrino emissivity throughout the NS core at a temperature $T = 3 \times 10^8$ K. The emissivity of non-superfluid matter is shown by the thick line. The jump by about 7 orders of magnitude is associated with the direct Urca threshold, ρ_D . The NSs with the central density $\rho_c < \rho_D$ have no kernels with the enhanced neutrino emission and show *slow* cooling. The NSs with $\rho_c > \rho_D$ will have these kernels and show *fast* cooling. The presence of the kernels has dramatic effects on the NS cooling (Lattimer et al. 1991).

4.2. The effects of superfluidity on neutrino emission

First we discuss the effects of superfluidity in the NS cores. The adopted models of proton and neutron critical temperatures (Sect. 3) in the core are shown in Figs. 1 and 2. The appropriate neutrino emissivities are displayed in Fig. 3. A proton superfluidity drastically changes the density profiles of the neutrino emissivity, $Q(\rho)$, as compared with the non-superfluid case (lines 1p, 2p, and 3p in Figs. 2 and 3).

At not too high density, $\rho \lesssim \rho_I$ (the threshold density ρ_I is specified in Sect. 6), a strong proton superfluidity almost switches off all neutrino processes involving protons, particularly, modified Urca process and even the most powerful direct Urca process. In this regime, the main neutrino emission is provided by neutrino-pair bremsstrahlung in neutron-neutron scattering; its level is *lower* than in a slowly cooling non-superfluid NS regulated by non-suppressed modified Urca process. Since strong proton superfluidity 3p extends to higher ρ , this regime persists to higher ρ , for this superfluidity.

At rather high $\rho \gtrsim \rho_{II}$ (the value ρ_{II} is also specified in Sect. 6) the proton superfluidity dies out and we have the neutrino emissivity fully enhanced by direct Urca process. Again, ρ_{II} is higher for proton superfluidity 3p.

At $\rho_I \lesssim \rho \lesssim \rho_{II}$ the neutrino emissivity is determined by direct Urca process partly suppressed by proton superfluidity. Evidently, this regime is absent in non-superfluid NSs. In this regime, the emissivity is sensitive to the decreasing slope of the $T_{\text{cp}}(\rho)$ profile and to EOS in the NS core.

Thus, in any $Q(\rho)$ profile, we can distinguish three distinctly different parts: (I) $\rho \lesssim \rho_I$; (II) $\rho_I \lesssim \rho \lesssim \rho_{II}$; (III) $\rho \gtrsim \rho_{II}$. They will lead (Sect. 6) to three types of cooling superfluid NSs.

Now we switch on neutron superfluidity in the core (model 1nt) in addition to the proton one. For $T = 3 \times 10^8$ K, this superfluidity occurs in a density range from $\sim 3 \times 10^{14}$ g cm $^{-3}$ to $\sim 6 \times 10^{14}$ g cm $^{-3}$ (Fig. 2). It creates a powerful splash of neutrino emission associated with Cooper pairing of neutrons as shown in Fig. 3 by the dotted line. This splash is actually the same for any model of proton superfluidity (1p, 2p, or 3p).

In addition, we discuss the effects of the neutron superfluidity in the crust. The density profiles of the critical

Table 3. Surface temperatures of eight isolated middle-aged neutron stars inferred from observations

Source	lg t [yr]	lg T_s^∞ [K]	Model ^{a)}	Confid. level	References
RX J0822–43	3.57	$6.23^{+0.02}_{-0.02}$	H	95.5%	Zavlin et al. (1999)
1E 1207–52	3.85	$6.10^{+0.05}_{-0.06}$	H	90%	Zavlin et al. (1998)
RX J0002+62	3.95 ^{b)}	$6.03^{+0.03}_{-0.03}$	H	95.5%	Zavlin & Pavlov (1999)
PSR 0833–45 (Vela)	4.4 ^{c)}	$5.83^{+0.02}_{-0.02}$	H	68%	Pavlov et al. (2001)
PSR 0656+14	5.00	$5.96^{+0.02}_{-0.03}$	bb	90%	Possenti et al. (1996)
PSR 0633+1748 (Geminga)	5.53	$5.75^{+0.05}_{-0.08}$	bb	90%	Halpern & Wang (1997)
PSR 1055–52	5.73	$5.88^{+0.03}_{-0.04}$	bb	^{d)}	Ögelman (1995)
RX J1856–3754	5.95	$5.72^{+0.05}_{-0.06}$	^{e)}	^{d)}	Pons et al. (2002)

^{a)} Observations are interpreted either with a hydrogen atmosphere model (H), or with a black body spectrum (bb)

^{b)} The mean age taken according to Craig et al. (1997).

^{c)} According to Lyne et al. (1996).

^{d)} Confidence level is uncertain.

^{e)} Analytic fit with Si-ash atmosphere model of Pons et al. (2002).

temperature $T_{\text{cns}}(\rho)$ (models 1ns, 2ns, and 3ns; Table 2; Figs. 1 and 4) and the appropriate neutrino emissivities $Q(\rho)$ at $T = 3 \times 10^8$ K are shown in Fig. 5. The thick line in Fig. 5 exhibits the emissivity of the non-superfluid crust provided mainly by neutrino-pair bremsstrahlung in electron-nucleus scattering. One can observe strong additional peaks of neutrino emission from superfluid crust produced by Cooper pairing of neutrons. The peaks are very sensitive to the models of $T_{\text{cns}}(\rho)$. However, since the NS crust contains a small fraction of NS mass (about 1–5 % or smaller, for the adopted NS models) this additional neutrino emission is important only in those NSs (Sect. 6.3) whose cores produce low neutrino luminosity.

4.3. Accreted surface layers

A heat-blanketing envelope (Sect. 2) is traditionally assumed to be made of iron (e.g., Gudmundsson et al. 1983). However, the envelope may partly contain light elements (H, He) provided, for instance, by accretion. In the heat-blanketing layers, the heat is mainly carried by degenerate electrons. The thermal conductivity of electrons which scatter off light ions is higher than the conductivity limited by scattering off iron ions. Thus, the accreted envelope is more heat transparent. The appropriate $T_s - T_b$ relationship was calculated by Potekhin et al. (1997). It depends on ΔM , the mass of accreted hydrogen or helium. The calculation takes into account nuclear burning of light elements in a hot and/or dense plasma, i.e., ΔM is the total accreted mass which may partly be processed into heavier elements due to nuclear transformations in accreted mat-

ter. The dependence of the photon NS luminosity on ΔM for four values of the temperature at the bottom of the heat-blanketing envelope ($T_b = 3 \times 10^7$, 10^8 , 3×10^8 , and 10^9 K) is shown in Fig. 6. If the heat-blanketing envelope is fully replaced by accreted material, the NS luminosity can increase by about one order of magnitude, i.e., the surface temperature T_s can increase by a factor of 2.

4.4. Surface magnetic field

The effects of strong magnetic field on the heat conduction through the blanketing NS envelope have been reviewed, for instance, by Ventura & Potekhin (2001). These effects depend on ρ , T , and the field strength B . One can distinguish (i) *classical effects* of electron Larmor rotation, and (ii) the *effects of quantization* of electron orbits across the field lines (Landau states).

The classical effects require lower magnetic fields. They become pronounced at $\omega_g \tau \gtrsim 1$, where ω_g is the electron gyrofrequency, and τ is the effective electron relaxation time. Then the conduction becomes anisotropic. The electron thermal conductivity along the field lines remains equal to its non-magnetic value κ_0 , while the conductivity in the perpendicular direction becomes $\kappa_0/[1 + (\omega_g \tau)^2]$.

The conditions of electron quantization are determined by characteristic density ρ_B and temperature T_B ,

$$\rho_B \approx 7.045 \times 10^3 (A/Z) B_{12}^{3/2} \text{ g cm}^{-3}, \quad (7)$$

$$T_B \approx \frac{1.343 \times 10^8 B_{12}}{\sqrt{1 + 1.018(\rho_6 Z/A)^{2/3}}} \text{ K}, \quad (8)$$

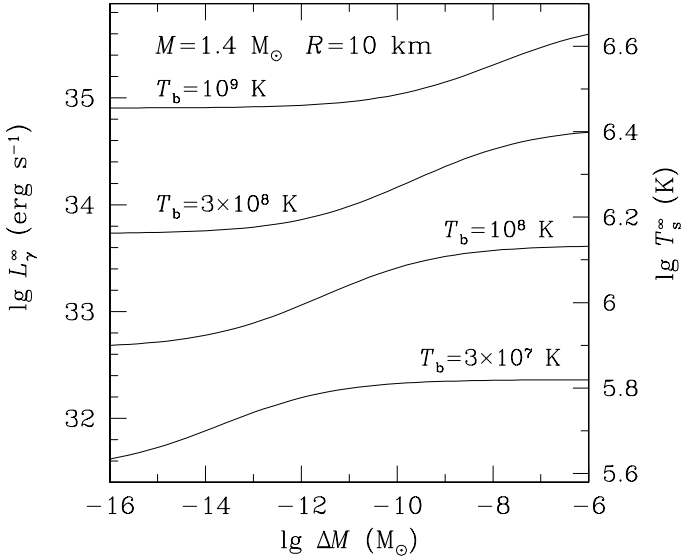


Fig. 6. Photon surface luminosity (redshifted as detected by a distant observer, left vertical axis) or redshifted effective surface temperature (right vertical axis) of a “canonical” NS model ($M = 1.4 M_\odot$, $R = 10$ km) for four values of the “internal” temperature T_b (at the bottom of the heat blanketing layer, $\rho_b = 10^{10}$ g cm $^{-3}$) versus the mass of accreted material, ΔM .

where Z is the mean charge number of atomic nuclei, A is the number of nucleons per a nucleus, $\rho_6 = \rho/10^6$ g cm $^{-3}$, and $B_{12} = B/10^{12}$ G. The magnetic field remains non-quantizing as long as $T \gg T_B$.

If $\rho \gtrsim \rho_B$ and $T \lesssim T_B$, then the magnetic field acts as *weakly quantizing*. In this regime, the conductivities exhibit de Haas – van Alphen oscillations around their classical values. The field becomes *strongly quantizing* at $\rho \lesssim \rho_B$ and $T \lesssim T_B$; it substantially modifies all components of the conductivity tensors well as the equation of state.

The thermal structure of the NS envelopes composed of iron at B up to 10^{16} G was studied, e.g., by Potekhin & Yakovlev (2001). Consider, for instance, the dipole field. Near the magnetic pole, the heat is carried away from the NS interior along the field lines. The electron-quantization effects amplify this conduction and make the polar regions of the heat-blanketing envelope more heat-transparent, increasing the local effective surface temperature for a given T_b . On the contrary, near the magnetic equator the heat propagates across the magnetic field. If $\omega_g \tau \gg 1$, the classical Larmor-rotation effects strongly reduce the corresponding transverse conductivity. The equatorial regions become less heat transparent, which lowers the local effective temperature for a given T_b . In an arbitrary element of the envelope, the heat conduction is affected by

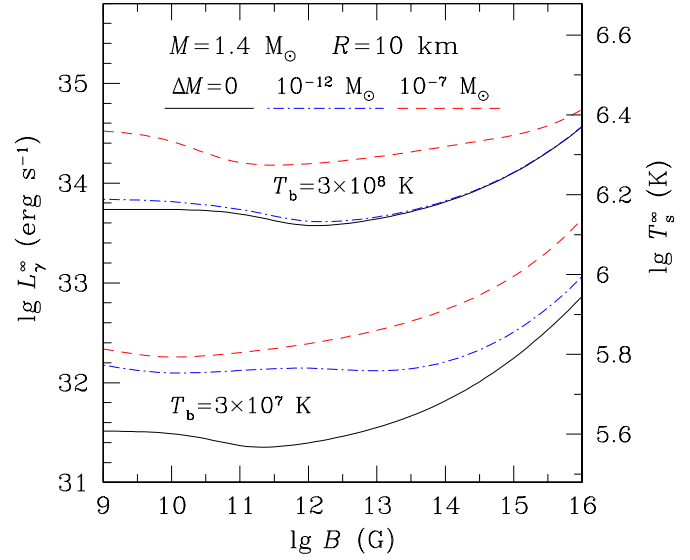


Fig. 7. Redshifted photon surface luminosity (left vertical axis) and mean effective temperature (right vertical axis) of a “canonical” NS with a dipole magnetic field, for two values of T_b and three models of the heat-blanketing envelope (accreted mass $\Delta M = 0$, $10^{-12} M_\odot$, and $10^{-7} M_\odot$) versus magnetic field strength B at the magnetic pole.

both (longitudinal and transverse) conductivities. The NS photon luminosity is obtained by integration of the local radiated flux over the entire NS surface – see Potekhin & Yakovlev (2001) and references therein for the case of the envelopes composed of iron. Here, we supplement these results with new results obtained for partly accreted envelopes with magnetic fields. The details of the new calculations will be presented elsewhere. Figure 7 displays the photon luminosity versus B for two selected values of T_b and three selected values of ΔM . The magnetic field affects the luminosity at $B \gtrsim 3 \times 10^{10}$ G. In the range of B up to $B \sim 3 \times 10^{13}$ G, the equatorial decrease of the heat transport dominates, and the NS luminosity is lower than at $B = 0$. For higher B , the polar increase of the heat transport becomes more important, and the magnetic field increases the photon luminosity. The variation of the photon luminosity by the magnetic field $B \lesssim 10^{15}$ G does not exceed a factor of 30.

The joint effect of the accreted envelope and the magnetic field is demonstrated by the dot-dashed and dashed lines. As in the non-magnetic case, the accreted material makes the envelope more heat-transparent, thus increasing the luminosity at given T_b . Therefore, at $B \sim 10^{10}$ – 10^{13} G, the magnetic field and the accreted envelope affect the thermal insulation in opposite directions. At higher field strengths, both effects increase the luminosity. However, as evident from Fig. 7, the dependence of this increase on

B and ΔM is complicated. In particular, at $B \gtrsim 10^{14}$ G, the effect of the accreted envelope is generally weaker than in the non-magnetic case.

5. Observational data

We will confront theoretical cooling curves with the results of observations of thermal emission from eight middle-aged isolated NSs. In discussing the observations and their theoretical interpretation we closely follow the consideration in KYG.

The observational data are the same as KYG. They are summarized in Table 3 and displayed in Figs. 8–13. The three youngest objects (RX J0822–43, 1E 1207–52, and RX J0002+62) are radio-quiet NSs in supernova remnants. The oldest object, RX J1856–3754, is also a radio-quiet NS. The other objects, Vela, PSR 0656+14, Geminga, and PSR 1055–52, are observed as radio pulsars. The NS ages are either pulsar spindown ages or the estimated supernova ages. The age of RX J1856–3754 was estimated by Walter (2001) from the kinematical data (by identifying a possible companion in the binary system existed before the supernova explosion). We use the value $t = 9 \times 10^5$ yr mentioned in the subsequent publication by Pons et al. (2002).

For the four youngest sources, the effective surface temperatures T_s^∞ are obtained from the observed X-ray spectra using hydrogen atmosphere models. Such models are more consistent (e.g., Pavlov & Zavlin 2002) with other information on these sources (distances, hydrogen column densities, inferred NS radii, etc.) than the blackbody model of NS emission. On the contrary, for the next three sources we present the values of T_s^∞ inferred using the blackbody spectrum because the blackbody model is more consistent for these sources. Finally, for RX J1856–3754 we adopt the values inferred using the analytic fit with Si-ash atmosphere model of Pons et al. (2002). We expect that the large error bar of T_s^∞ provided by this model reflects poor understanding of thermal emission from this source (e.g., Pons et al. 2002, Burwitz et al. 2001, Gänsicke et al. 2001, Kaplan et al. 2001, Pavlov et al. 2002).

6. Theory and observations

6.1. Non-superfluid neutron stars

There is a large scatter of observational limits on T_s^∞ for the eight sources. Three sources, the youngest RX J0822–43, and two oldest, PSR 1055–52 and RX J1856–3754, seem to be hot for their ages, while the other ones, especially Vela and Geminga, look much colder. We can interpret all observational data with the cooling curves using the fixed (the same) EOS and models of the critical temperatures $T_c(\rho)$ (Sect. 3) for all objects. The results are presented in Figs. 8–13.

In the *absence of any superfluidity* there are *two* well-known, distinctly different cooling regimes, *slow* and *fast*

cooling. The slowly cooling NSs have low masses, $M < M_D$. They mainly lose their energy via neutrino emission in modified Urca processes. For given EOSs in the NS core, the cooling curves of middle-aged NSs are almost the same for all M from about M_\odot to M_D (e.g., Page & Applegate 1992, Gnedin et al. 2001), being not very sensitive to EOS. The fast cooling occurs via a very powerful direct Urca process (Lattimer et al. 1991) if $M > M_D + 0.003 M_\odot$. The cooling curves are again not too sensitive to the mass and EOS. The middle-aged rapidly cooling NSs are much colder than the slowly cooling ones. Two examples, 1.35 and 1.5 M_\odot non-superfluid NSs (EOS A), are displayed in Fig. 8. The transition from the slow to fast cooling takes place in a very narrow mass range, $M_D < M \lesssim M_D + 0.003 M_\odot$. In order to explain these observational limits with the non-superfluid NS models one should make an unlikely assumption that at least the masses of the Vela and Geminga pulsars fall in that narrow mass range. Thus, several sources exhibit the intermediate case between the slow and fast cooling. In the absence of superfluidity, this is highly unlikely.

6.2. Proton superfluidity and the three types of cooling neutron stars

The next step is to interpret the observations (Fig. 9–13) by cooling of superfluid NSs. It turns out that various superfluids affect NS cooling in different ways. Our main assumptions would be that the *proton superfluidity is rather strong* at $\rho \lesssim \rho_D$, while the *3P_2 neutron superfluidity is rather weak* (Sect. 6.4). We start with the effects of proton superfluidity.

The dot-and-dashed cooling curves in Figs. 9–11 are computed assuming the proton superfluidity alone. The proton pairing 1p is adopted in Fig. 9, 2p in Fig. 10, and 3p in Fig. 11. EOS A is used in the models in Figs. 9 and 10, and EOS B in Fig. 11.

As seen from Figs. 9–11, the proton superfluidity leads to the *three* cooling regimes (instead of two in non-superfluid NSs): *slow*, *moderate*, and *fast*. They reflect three neutrino emission regimes from the NS cores discussed in Sect. 4.2 (Fig. 3). Accordingly, there are *three types* of cooling NSs with distinctly different properties.

(I) *Low-mass, slowly cooling* NSs. Their central densities ρ_c and masses $M = M(\rho_c)$ obey the inequalities

$$\rho_c \lesssim \rho_I, \quad M \lesssim M_I = M(\rho_I), \quad (9)$$

where ρ_I , introduced in Sect. 4.2, is discussed below in more detail.

(II) *Medium-mass, moderately cooling* NSs, with

$$\rho_I \lesssim \rho_c \lesssim \rho_{II}, \quad M_I \lesssim M \lesssim M_{II} = M(\rho_{II}), \quad (10)$$

where ρ_{II} , also introduced in Sect. 4.2, is specified below.

(III) *Massive, rapidly cooling* NSs,

$$\rho_{II} \lesssim \rho_c \leq \rho_{\text{cmax}}, \quad M_{II} \lesssim M \leq M_{\text{max}}, \quad (11)$$

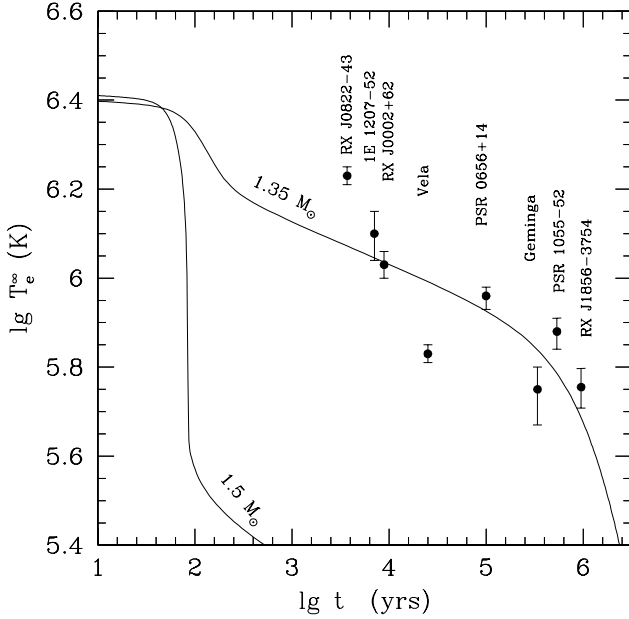


Fig. 8. Observational limits on surface temperatures of eight NSs (Table 3) compared with cooling curves of non-superfluid NSs (EOS A) of $M = 1.35$ and $1.5 M_{\odot}$.

where ρ_{cmax} and M_{max} refer to the maximum-mass configuration (Table 1).

The threshold values of $\rho_{\text{I,II}}$ and $M_{\text{I,II}}$ depend on a proton superfluidity model $T_{\text{cp}}(\rho)$, EOS in the NS core, and on a NS age. The main properties of regimes I, II, and III are as follows.

(I) *The slowly cooling NSs* are those where the direct Urca process is either forbidden by momentum conservation ($\rho_{\text{c}} \leq \rho_{\text{D}}$) or greatly suppressed by the strong proton superfluidity (Fig. 3).

In particular, the cooling is slow for $\rho_{\text{c}} < \rho_{\text{D}}$ and $M < M_{\text{D}}$ in the absence of proton superfluidity. This is the well-known *ordinary slow cooling* which is mainly regulated by the neutrino emission produced by the modified Urca process (Sect. 6.1). However, for the conditions displayed in Figs. 9–11, the proton superfluidity in regime I is so strong that it almost switches off both, the modified Urca process everywhere in the NS core and the direct Urca process at $\rho > \rho_{\text{D}}$. Then the neutrino emission is mainly produced by neutrino bremsstrahlung in neutron-neutron scattering (Sect. 4.2) unaffected by the neutron superfluidity in the NS core (that is assumed to be weak). The bremsstrahlung is less efficient than the modified Urca process and leads to a slower cooling than in a non-superfluid NS. It can be referred to as the *very slow cooling*.

The analysis shows (KYG) that, for the selected models, the regime of very slow cooling holds as long as the

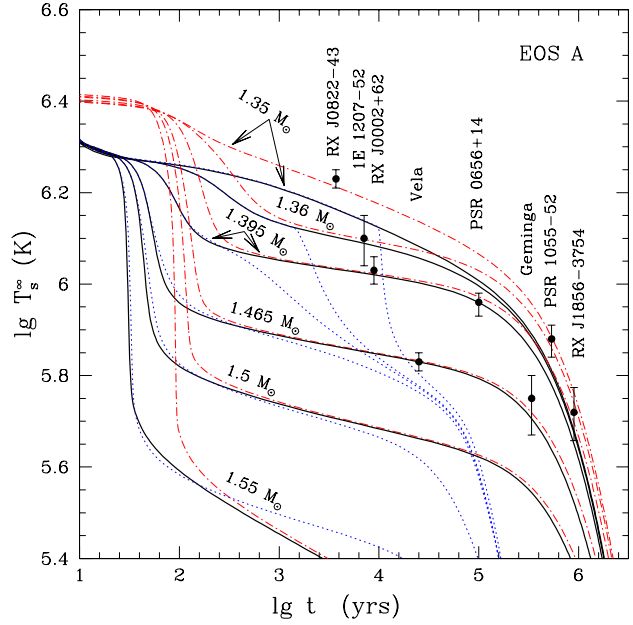


Fig. 9. Observational limits on surface temperatures of eight NSs compared with cooling curves of NSs (EOS A) with masses from 1.35 to $1.55 M_{\odot}$ (after KYG). Dot-and-dashed curves are obtained including proton superfluidity 1p alone. Solid curves include, in addition, model 1ns of neutron superfluidity. Dotted lines also take into account the effect of neutron superfluidity 1nt.

proton critical temperature in the NS center is higher than a threshold value:

$$T_{\text{cp}}(\rho_{\text{c}}) \gtrsim T_{\text{cp}}^{(1)}(\rho_{\text{c}}). \quad (12)$$

Comparing the neutrino emissivities of the indicated reactions (e.g., Yakovlev et al. 1999), KYG obtained the simple estimates: $T_{\text{cp}}^{(1)}(\rho) \sim 5.5 T$ for $\rho \leq \rho_{\text{D}}$, and $T_{\text{cp}}^{(1)}(\rho) \sim 17 T$ for any ρ which is several per cent higher than ρ_{D} , where T is the internal NS temperature. There is a continuous transition (Fig. 9 in KYG) between the presented values of $T_{\text{cp}}^{(1)}(\rho)$ in the narrow density range near ρ_{D} .

To make the analysis less abstract we notice that in a very slowly cooling NS the internal temperature is $T \sim 5.5 \times 10^8$, 4×10^8 , and 1.5×10^8 K at $t \sim 4 \times 10^3$, 2.5×10^4 , and 4×10^5 yr, respectively.

Now we can explicitly specify the maximum central densities ρ_{I} and masses M_{I} of very slowly cooling NSs in Eq. (9) for the cases of study, in which $\rho_{\text{I}} \gtrsim \rho_{\text{D}}$ ($M_{\text{I}} \gtrsim M_{\text{D}}$). If $\rho_{\text{c}} > \rho_{\text{D}}$, then we can define ρ_{I} as the density value on the decreasing, high-density slope of $T_{\text{cp}}(\rho)$ (Figs. 1 and 2) which corresponds to $T_{\text{cp}}(\rho_{\text{I}}) = T_{\text{cp}}^{(1)}(\rho_{\text{I}})$. It gives the central density of the NS and $M_{\text{I}} = M(\rho_{\text{I}})$.

For the conditions displayed in Figs. 9–11, the cooling curves (dot-and-dashed lines) of all low-mass NSs with any proton superfluidity (1p, 2p, or 3p) are very similar. For instance, the $1.35 M_{\odot}$ curve in Fig. 3 is plotted just as an

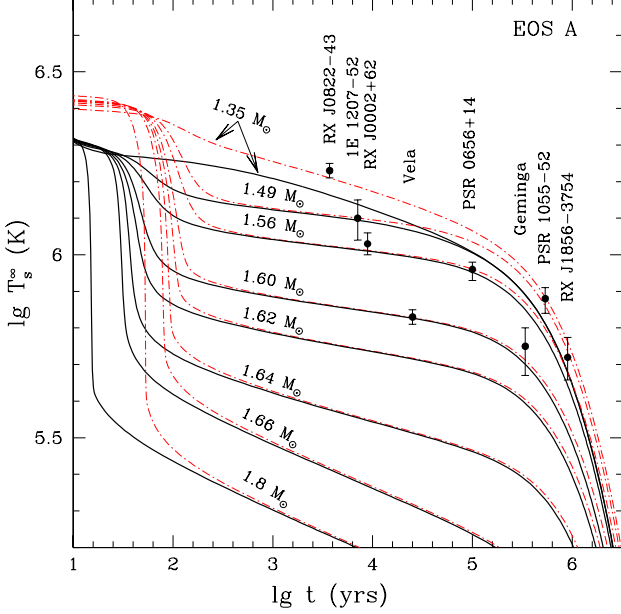


Fig. 10. Observational limits on surface temperatures of NSs compared with cooling curves of NSs (EOS A) with several masses M in the presence of proton superfluidity 2p (from KYG). Dot-and-dashed curves are obtained assuming non-superfluid neutrons. Solid curves include, in addition, model 1ns of neutron superfluidity. $^3\text{P}_2$ neutron pairing is neglected.

example; all the curves are almost identical in the mass range $M_\odot \lesssim M < M_I$. Moreover, the cooling curves are not too sensitive to EOS and are *insensitive to the exact values of the proton critical temperature* T_{cp} , as long as the inequality (12) holds. These curves are noticeably higher than the curves which describe the ordinary slow cooling in the absence of superfluidity (e.g., Fig. 8). It is remarkable that they seem to be almost model-independent.

For the conditions in Figs. 9–11, the three relatively hot sources, RX J0822–43, PSR 1055–52, and RX J1856–3754, can be treated as these very-slow-cooling (low-mass) models.

(II) *The moderately cooling stars* are the NSs which possess central kernels where the direct Urca process is allowed but moderately suppressed by proton superfluidity. The existence of a representative class of these NSs is solely due to proton superfluidity.

According to KYG, for the selected cooling models, the proton critical temperature in the center of a medium-mass NS should roughly satisfy the inequality

$$T_{\text{cp}}^{(\text{II})}(\rho_{\text{c}}) \lesssim T_{\text{cp}}(\rho_{\text{c}}) \lesssim T_{\text{cp}}^{(\text{I})}(\rho_{\text{c}}), \quad (13)$$

with $T_{\text{cp}}^{(\text{II})} \sim 3T$. Thus, one can find ρ_{II} which corresponds to $T_{\text{cp}}(\rho_{\text{II}}) = T_{\text{cp}}^{(\text{II})}(\rho_{\text{II}})$ and determines M_{II} , the maximum mass of moderately cooling NSs in Eq. (10).

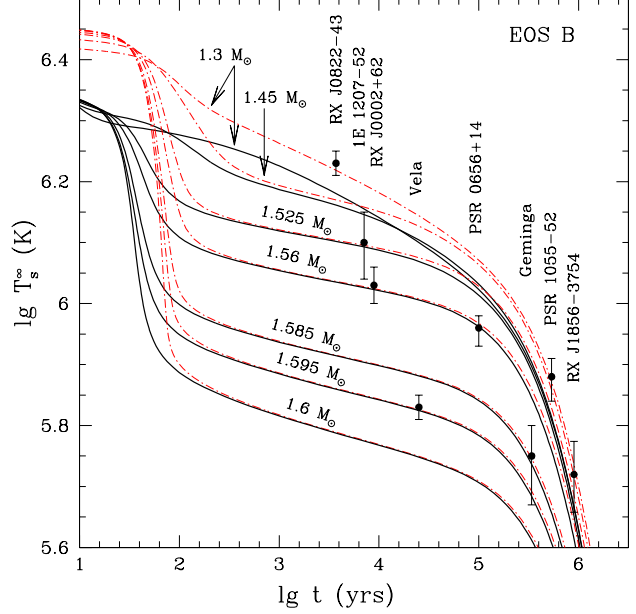


Fig. 11. Observational limits on surface temperatures of NSs compared with cooling curves of NSs (EOS B) with masses from 1.3 to 1.6 M_\odot (from KYG). Dot-and-dashed curves are obtained using model 3p of proton superfluidity. Solid curves include, in addition, model 1ns of neutron superfluidity.

The surface temperatures of these medium-mass NSs are governed by proton superfluidity in the NS central kernels, $\rho \gtrsim \rho_{\text{I}}$. One can observe (Figs. 9–11) a steady decrease of the surface temperatures with increasing M . Fixing the proton superfluidity and EOS, one can determine (Kaminker et al. 2001 and Yakovlev et al. 2001b) the masses of moderately cooling NS, which means “weighing” NSs. In this fashion one can weigh five isolated NSs (1E 1207–52, RX J0002+62, Vela, PSR 0656+14, and Geminga) as shown in Figs. 9–11. For instance, adopting EOS A and proton superfluid 1p (Fig. 9) KYG obtain the masses in the range from $\approx 1.36 M_\odot$ (for 1E 1207–52) to $\approx 1.465 M_\odot$ (for Vela and Geminga). For EOS A and proton superfluid 2p (Fig. 10) KYG obtain higher masses of the same sources. Obviously, the properties of moderately cooling NSs are *extremely sensitive* to the decreasing slope of $T_{\text{cp}}(\rho)$ in the density range from ρ_{I} to ρ_{II} (and insensitive to the details of $T_{\text{cp}}(\rho)$ outside this range).

(III) *Massive* NSs show *fast* cooling similar to the fast cooling of non-superfluid NSs. These stars have central kernels where the direct Urca process is either unaffected or weakly suppressed by the proton superfluidity. In such kernels, $T_{\text{cp}}(\rho) \lesssim T_{\text{cp}}^{(\text{II})}$. The central densities and masses of these NSs lie in the range given by Eq. (11). Their thermal evolution is not very sensitive to the model of $T_{\text{cp}}(\rho)$ and to EOS in the stellar core. Note that if $\rho_{\text{cmax}} < \rho_{\text{II}}$, the rapidly cooling NSs do not exist. In the frame of

this interpretation, no NS observed so far can be assigned to this class.

6.3. Crustal superfluidity and slow cooling

At the next step, we retain proton superfluidity and add $^1\text{S}_0$ neutron superfluidity 1ns in the NS crust. These models are shown by the solid curves in Figs. 9–11. For the moderately or rapidly cooling middle-aged NSs, they are fairly close to the dot-and-dashed curves. This is quite expected (e.g., Gnedin et al. 2001): the $^1\text{S}_0$ neutron superfluidity is mainly located in the NS crust which is much less massive than the NS core. Thus, the crustal superfluidity does not affect noticeably the proposed interpretation of 1E 1207–43, RX J0002+62, Vela, PSR 0656+14, and Geminga in terms of moderately cooling NSs.

However, as pointed out by Yakovlev et al. (2001b), this crustal superfluidity strongly affects the slow cooling of low-mass NSs, and the effects are twofold. First, at $t \lesssim 3 \times 10^5$ yr the neutrino luminosity due to $^1\text{S}_0$ pairing of neutrons may dominate the sufficiently low neutrino luminosity of the stellar core. Second, at $t \gtrsim 10^5$ yr the $^1\text{S}_0$ neutron superfluidity reduces the heat capacity of the crust. Both effects accelerate NS cooling and decrease T_s^∞ (Figs. 9–11) violating the interpretation of the three sufficiently hot sources, RX J0822–43, PSR 1055–52, and RX J1856–3754. The interpretation of RX J1856–3754 is affected to a lesser extent, as a consequence of the rather large error bar of T_s^∞ for this source (Sect. 5).

However, the interpretation can be rescued by the appropriate choice of $T_{\text{cns}}(\rho)$. It is sufficient to focus on the interpretation of RX J0822–43, PSR 1055–52, and RX J1856–3754, as the very slowly cooling NSs. For certainty, we take EOS B, $M = 1.3 M_\odot$, and proton superfluid 3p. The results are presented in Figs. 12 and 13. The dot-and-dashed line is the same as in Fig. 11 and neglects the crustal neutron superfluidity. Thick solid line is also the same as in Fig. 11. It includes an additional effect of crustal superfluid 1ns and lies below the observational limits on T_s^∞ for the sources in question (or almost below in case of RX J1856–3754). To keep the proposed interpretation of the three sources one must raise the cooling curves calculated including the crustal superfluidity. To this aim, one should suppress the neutrino emission associated with $^1\text{S}_0$ pairing of neutrons (Fig. 5). Recall that in a middle-aged NS this emission is mainly generated (Fig. 5) in two relatively narrow layers, near the neutron drip point and near the crust-boundary interface, where the local NS temperature T is just below $T_{\text{cns}}(\rho)$. Since the Cooper-pairing neutrino luminosity is roughly proportional to the widths of these emitting layers, one can reduce the luminosity by reducing the widths. This can be done by setting $T_{\text{cns}}^{\text{max}}$ higher and by making the sharper decrease of $T_{\text{cns}}(\rho)$ in the wings.

For example, taking crustal superfluid 2ns instead of 1ns (Figs. 4 and 5) one obtains the dashed cooling curve

in Fig. 12 which comes much closer to the dot-and-dashed curve than the thick solid curve (model 1ns). Note that the cooling curves are insensitive to the details of $T_{\text{cns}}(\rho)$ profile near the maximum, as long as $T_{\text{cns}}^{\text{max}} \gtrsim 5 \times 10^9$ K, but they are extremely sensitive to the decreasing slopes of $T_{\text{cns}}(\rho)$. On the other hand, by taking the smoother and lower $T_{\text{cns}}(\rho)$, model 3ns, one obtains a colder NS than needed for the interpretation of the observations (long-dash line in Fig. 12). Therefore, $^1\text{S}_0$ neutron superfluidity with maximum $T_{\text{cns}}^{\text{max}} < 5 \times 10^9$ K and/or with smoothly decreasing slopes of the $T_{\text{cns}}(\rho)$ profile near the crust-core interface and the neutron drip point *violates* the proposed interpretation of the observational data.

Moreover, the observations of RX J0822–43, PSR 1055–52, and RX J1856–3754 can be fitted even with the initial model 1ns of the crustal superfluidity (Fig. 13). The high surface temperature of RX J0822–43 can be explained assuming additionally the presence of a low-mass ($2 \times 10^{-11} M_\odot$) heat-blanketing surface envelope of hydrogen or helium. This effect is modeled using the results of Potekhin et al. (1997) described in Sect. 4 (Fig. 6). Light elements raise T_s^∞ at the neutrino cooling stage (curve *acc* in Fig. 13). In order to explain the observations of PSR 1055–52 and RX J1856–3754, one can assume again model 1ns of crustal superfluidity, iron surface and the dipole surface magnetic field ($\sim 10^{12}$ G at the magnetic pole; line *mag* in Fig. 13). Such a field makes the NS surface layers overall less heat-transparent (Fig. 7), rising T_s^∞ at $t \gtrsim 3 \times 10^5$ yr. Note that the dipole field $\gtrsim 3 \times 10^{13}$ G has the opposite effect, resembling the effect of the surface envelope of light elements.

To summarize, one can additionally vary cooling curves by assuming the presence of light elements and the magnetic field on the NS surface (line *acc-mag* in Fig. 13). However, these variations are less pronounced than those due to nucleon superfluidity. For instance, one cannot reconcile the cooling curves with the present observations of PSR 1055–52 assuming model 3ns of the crustal superfluidity with any surface magnetic field.

6.4. $^3\text{P}_2$ pairing of neutrons in the NS core

Now we focus on the $^3\text{P}_2$ neutron pairing neglected so far. Its effects are illustrated in Fig. 9, as an example. They are qualitatively similar for the other cooling models in Figs. 10 and 11. In Fig. 9 we take the cooling models obtained including proton superfluidity 1p and crustal superfluidity 1ns, and add the $^3\text{P}_2$ neutron superfluidity (model 1nt, Table 2) in the core. This gives the same (solid) cooling curves for the young NSs which have the internal temperatures T above the maximum value of $T_{\text{cnt}}^{\text{max}} \approx 3 \times 10^8$ K. However, when T falls below $T_{\text{cnt}}^{\text{max}}$, one obtains (dots) a strong acceleration of the cooling associated with the powerful neutrino emission due to $^3\text{P}_2$ neutron pairing (Fig. 3). This emission greatly complicates the proposed interpretation of older sources, PSR 0656+14, Geminga, PSR

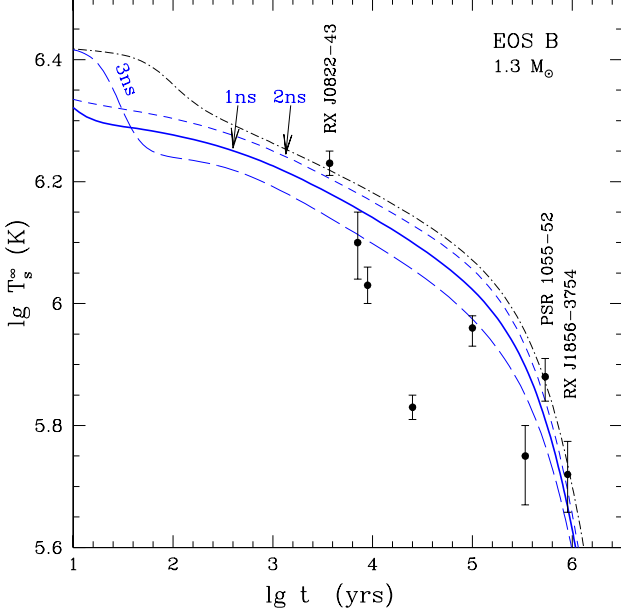


Fig. 12. Cooling curves of $1.3 M_{\odot}$ NS model (EOS B) versus observations of RX J0822-43, PSR 1055-52, and RX J1856-3754 (after KYG). Dot-and-dashed curve: proton superfluidity 3p in the NS core. Solid, short-dashed, and long-dashed curves include, in addition, models 1ns, 2ns, and 3ns of crustal neutron superfluidity, respectively. Thick solid line is the same as in Fig. 11.

1055-52, and RX J1856-3754. The complication arises for a wide class of $T_{\text{cnt}}(\rho)$ profiles with $T_{\text{cnt}}^{\text{max}}$ from $\sim 10^8$ K to $\sim 3 \times 10^9$ K (in this way, it can be regarded as model-independent). The Cooper-pairing neutrino emission of neutrons induces *really fast cooling* of older sources even if their mass is *low*, $M < M_D$ (Sect. 6.2). To avoid this difficulty one can assume (Kaminker et al. 2001) *weak* 3P_2 pairing, $T_{\text{cnt}}(\rho)$, with maximum $T_{\text{cnt}}^{\text{max}} < 10^8$ K; it does not affect the proposed interpretation.

7. Summary

Following KYG we summarize the effects superfluids on NS cooling.

(a) Strong proton superfluidity in the NS cores, combined with the direct Urca process at $\rho > \rho_D$, separates (Sect. 6.2) the cooling models into three distinctly different types: (I) slowly cooling, low-mass NSs ($M \lesssim M_I$); (II) moderately cooling, medium-mass NSs ($M_I \lesssim M \lesssim M_{II}$); (III) rapidly cooling, massive NSs ($M \gtrsim M_{II}$). The regime of moderate cooling cannot be realized without the proton superfluidity.

(b) Strong proton superfluidity in the NS core is required to interpret the observational data on the three sources, RX J0822-43, PSR 1055-52, and RX J1856-3754, hot for their ages, as the very slowly cooling NSs (Sects.

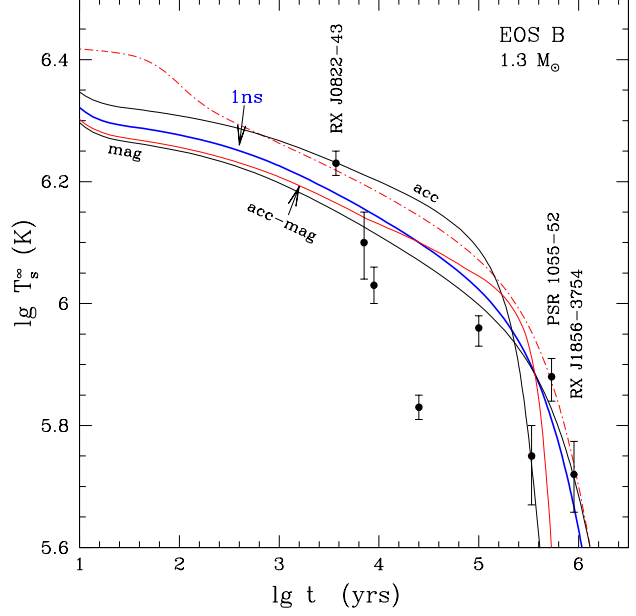


Fig. 13. Cooling curves of $1.3 M_{\odot}$ NS model versus observations of RX J0822-43, PSR 1055-52, and RX J1856-3754. Dot-and-dashed curve: proton superfluidity 3p in the NS core. Solid curves include, in addition, model 1ns of crustal neutron superfluidity. Thick solid line is the same as in Figs. 11 and 12. Thin solid curve *acc* is calculated assuming the presence of $2 \times 10^{-11} M_{\odot}$ of hydrogen on the NS surface. Thin solid curve *mag* is obtained assuming the iron surface and dipole magnetic field (10^{12} G at the magnetic pole). Thin solid curve *acc-mag* is obtained assuming both, the magnetic field (10^{12} G) and accreted envelope ($2 \times 10^{-11} M_{\odot}$).

6.2 and 6.3). Within this interpretation, all three sources may have masses from about M_{\odot} to M_I ; one cannot determine their masses exactly or distinguish EOS in the NS core from the cooling models.

(c) Strong proton superfluidity is needed to interpret observations of the other sources, 1E 1207-52, RX J0002+62, Vela, PSR 0656+14, and Geminga, as the medium-mass NSs. One can “weigh” these NSs, i.e., determine their masses, for a given model of $T_{\text{cp}}(\rho)$ and a given EOS. The weighing is very sensitive to the decreasing slope of $T_{\text{cp}}(\rho)$ in the density range $\rho_I \lesssim \rho \lesssim \rho_{II}$ (Sect. 6.2).

(d) Strong or moderate 3P_2 neutron superfluidity in the NS core initiates rapid cooling due to the neutrino emission resulted from neutron pairing. This would invalidate the proposed interpretation of the old sources like PSR 0656+14, Geminga, PSR 1055-52, and RX J1856-3754. One can save the interpretation assuming a weak 3P_2 neutron superfluidity, $T_{\text{cnt}}^{\text{max}} < 10^8$ K (Sect. 6.4).

(e) 1S_0 neutron superfluidity in the crust may initiate a strong Cooper-pairing neutrino emission, decrease

substantially T_s^∞ of the slowly cooling NSs, and weaken the interpretation of RX J0822–43, PSR 1055–52, and RX J1856–3754 (although it does not affect significantly the moderate or fast cooling). The interpretation can be saved by assuming that the maximum of $T_{\text{cns}}(\rho)$ is not too small ($T_{\text{cns}}^{\text{max}} \gtrsim 5 \times 10^9$ K) and the profile of $T_{\text{cns}}(\rho)$ decreases sharply in the wings (Sect. 6.3).

(f) The interpretation of the slowly cooling sources is sensitive to the presence of the surface magnetic fields and/or heat-blanketing surface layer composed of light elements (Sect. 6.3).

(g) No isolated middle-aged NSs observed so far can be identified as a rapidly cooling NS. In the frame of the proposed models, these NSs do not exist for those EOSs and $T_{\text{cp}}(\rho)$ profiles for which $M_{\text{max}} < M_{\text{II}}$.

If the proposed interpretation is correct, one can make the following conclusions on the properties of dense matter in NS interiors.

(i) Strong proton superfluidity is in favor of a not too large symmetry energy at supranuclear densities (Kaminker et al. 2001). A very large symmetry energy would mean a high proton fraction which would suppress proton pairing. On the other hand, the symmetry energy should be not too small to open the direct Urca process at $\rho > \rho_{\text{D}}$.

(ii) Weak ${}^3\text{P}_2$ neutron pairing is in favor of a not too soft EOS in the NS core (Kaminker et al. 2001). The softness would mean a strong attractive neutron-neutron interaction and, therefore, strong neutron pairing.

(iii) The adopted features of the crustal neutron superfluidity are in favor of those microscopic theories which predict $T_{\text{cns}}(\rho)$ profiles with $T_{\text{cns}}^{\text{max}} \gtrsim 5 \times 10^9$ K. This is in line with many microscopic calculations of the superfluid gaps which include the medium polarization effects in neutron-neutron interaction (e.g., Lombardo & Schulze 2001). However, the reduction of the gap by the medium polarization should not be too strong, and the decreasing slope of $T_{\text{cns}}(\rho)$ should be rather sharp. These requirements constrain the microscopic theories.

The proposed interpretation of the observations relates the inferred NS masses to the superfluid properties of NS interiors. By varying EOS and the proton critical temperature, one can attribute different masses to the same sources. If, on the other hand, one knew the range of masses of the cooling middle-aged NSs it would be possible to draw definite conclusions on the superfluid state of their interiors, first of all, on the proton critical temperature, $T_{\text{cp}}(\rho)$.

The presented analysis may seem too simplified because it neglects a possible presence of other particles in the NS cores (muons, hyperons, quarks). It is expected that the inclusion of other particles and the effects of superfluidity of hyperons or quarks will complicate theoretical analysis but will not change the basic conclusion on the existence of the slowly, moderately, and rapidly cooling NSs.

The calculations show that the cooling of middle-aged NSs with $M < M_{\text{I}}$ is sensitive to the density profile of free neutrons near the crust bottom and neutron drip point. The presented calculations used only one model of the free-neutron distribution in the crust, assuming spherical atomic nuclei at the crust bottom. It would be interesting to consider the models of crust matter with non-spherical nuclei (e.g., Pethick & Ravenhall 1995) and the effects of superfluidity of nucleons confined in the atomic nuclei in the NS crust.

The determination of T_s^∞ from observational data is a very complicated problem (as described, e.g., by Pavlov & Zavlin 2002). It requires very high-quality data and theoretical models of NS atmospheres. Thus, the current values of T_s^∞ may change substantially after the forthcoming observations and new theoretical modeling. These changes may affect the proposed interpretation of the observational data, first of all, of RX J0822–43, PSR 1055–52, and RX J1856–3754. For instance, RX J1856–3754 may have a colder surface ($T_s^\infty \sim 0.25$ MK), than assumed in the above analysis, with a hot spot (e.g., Pons et al. 2002, Burwitz et al. 2001, Gänsicke et al. 2001). If confirmed, the lower T_s^∞ might be explained by the effect of ${}^3\text{P}_2$ neutron pairing (Fig. 9).

The future observations of the thermal emission from these sources will be crucial for understanding the superfluid properties of NS matter.

The proposed theory can explain the existence of NSs within a broad range of T_s^∞ . However, it would be unable to explain too hot and too cold objects (with T_s^∞ essentially higher than the highest cooling curve and essentially lower than the lowest curve in Figs. 9–11). A discovery of such hot or cold isolated NSs would be of special interest.

Acknowledgements. One of the authors (DGY) gratefully acknowledges the support by the Heraeus foundation. We are grateful to G.G. Pavlov for encouragement, to M.E. Gusakov and K.P. Levenfish, for useful comments. The work was partially supported by RFBR (grants No. 02-02-17668 and 00-07-90183).

References

- Burwitz V., Zavlin V.E., Neuhäuser R., Predehl R., Trümper J., Brinkman A.C., 2001, *A&A* 327, L35
- Craig W.W., Hailey Ch.J., Pisarski R.L., 1997, *ApJ* 488, 307
- Gänsicke B.T., Braje T.M., Romani R.W., 2001, *A&A* (submitted, astro-ph/0110130)
- Gnedin O.Y., Yakovlev D.G., Potekhin A.Y., 2001, *MNRAS* 324, 725
- Gudmundsson E.H., Pethick C.J., Epstein R.I., 1983, *ApJ* 272, 286
- Flowers E.G., Ruderman M., Sutherland P.G., 1976, *ApJ* 205, 541
- Halpern J.P., Wang F.Y.-H., 1997, *ApJ* 477, 905
- Kaminker A.D., Haensel P., Yakovlev D.G., 2001, *A&A* 373, L17
- Kaminker A.D., Yakovlev D.G., Gnedin O.Y., 2002, *A&A* 383, 1076 (KYG)

- Kaplan D.L., van Kerkwijk M.H., Anderson J., 2001, ApJ (submitted; astro-ph/0111174)
- Lattimer J.M., Pethick C.J., Prakash M., Haensel P., 1991, Phys. Rev. Lett. 66, 2701
- Lattimer J.M., Van Riper K.A., Prakash M., Prakash M., 1994, ApJ 425, 802
- Lattimer J.M., Prakash M., 2001, ApJ 550, 426
- Lyne A.G., Pritchard R.S., Graham-Smith F., Camilo F., 1996, Nature 381, 497
- Lombardo U., Schulze H.-J., 2001, in *Physics of Neutron Star Interiors*, ed. D. Blaschke, N. Glendenning, A. Sedrakian (Springer, Berlin) p. 30
- Negele J.W., Vautherin D., 1973, Nucl. Phys. A207, 298
- Ögelman H., 1995, in *The Lives of the Neutron Stars*, ed. M.A. Alpar, Ü. Kiziloğlu, J. van Paradijs, NATO ASI Ser. C, vol. 450 (Kluwer, Dordrecht) p. 101
- Page D., 1998, in *The Many Faces of Neutron Stars*, NATO ASI Ser. C, vol. 515, ed. R. Buccheri, J. van Paradijs, M.A. Alpar (Kluwer, Dordrecht) p. 538
- Page D., Applegate J.H., 1992, ApJ 394, L17
- Pavlov G.G., Zavlin V.E., 2002, an invited talk at WE-Heraeus Seminar No. 270 (21–25 January 2002, Physikzentrum Bad Honnef, Germany)
- Pavlov G.G., Zavlin V.E., Sanwal D., Burwitz V., Garmire G.P., 2001, ApJ 552, L129
- Pavlov G.G., Sanwal D., Garmire G.P., Zavlin V.E., 2002, in *Neutron Stars in Supernova Remnants*, ed. P.O. Slane, B.M. Gaensler, ASP Conf. Ser. (accepted, astro-ph/0112322)
- Pethick C.J., Ravenhall D.G., 1995, Ann. Rev. Nucl. Particle Sci. 45, 429
- Pons J., Walter F., Lattimer J., Prakash M., Neuhäuser R., An P., 2002, ApJ 564, 981
- Possenti A., Mereghetti S., Colpi M., 1996, A&A 313, 565
- Potekhin A.Y., Chabrier G., Yakovlev D.G., 1997, A&A 323, 415
- Potekhin A.Y., Yakovlev G.G., 2001, A&A 374, 213
- Prakash M., Ainsworth T.L., Lattimer J.M., 1988, Phys. Rev. Lett. 61, 2518
- Shapiro S.L., Teukolsky S.A., 1983, *Black Holes, White Dwarfs, and Neutron Stars* (Wiley, New York)
- Thorne K.S., 1977, ApJ 212, 825
- Ventura J., Potekhin A.Y., 2001, in *The Neutron Star – Black Hole Connection*, NATO ASI Ser. C, v. 567, ed. C. Kouveliotou, J. Ventura, E. van den Heuvel (Kluwer, Dordrecht) 393
- Walter F.M., 2001, ApJ 549, 433
- Yakovlev D.G., Levenfish K.P., Shibano Yu.A., 1999, Physics–Uspekhi 42, 737 (astro-ph/9906456)
- Yakovlev D.G., Kaminker A.D., Gnedin O.Y., Haensel P., 2001a, Phys. Rep. 354, 1
- Yakovlev D.G., Kaminker A.D., Gnedin O.Y., 2001b, A&A 379, L5
- Zavlin V.E., Pavlov G.G., Trümper J., 1998, A&A 331, 821
- Zavlin V.E., Pavlov G.G., 1999, private communication
- Zavlin V.E., Trümper J., Pavlov G.G., 1999, ApJ 525, 959